



CHORUS

This is the accepted manuscript made available via CHORUS. The article has been published as:

# Elastic Instabilities Govern the Morphogenesis of the Optic Cup

Jeong-Ho Lee, Harold S. Park, and Douglas P. Holmes

Phys. Rev. Lett. **127**, 138102 — Published 23 September 2021

DOI: [10.1103/PhysRevLett.127.138102](https://doi.org/10.1103/PhysRevLett.127.138102)

# Elastic Instabilities Govern the Morphogenesis of the Optic Cup

Jeong-Ho Lee,<sup>1</sup> Harold S. Park,<sup>1,\*</sup> and Douglas P. Holmes<sup>1,†</sup>

<sup>1</sup>*Department of Mechanical Engineering, Boston University, Boston, MA, 02215.*

(Dated: August 9, 2021)

Because the normal operation of the eye depends on sensitive morphogenetic processes for its eventual shape, developmental flaws can lead to wide-ranging ocular defects. However, the physical processes and mechanisms governing ocular morphogenesis are not well understood. Here, using analytical theory and nonlinear shell finite-element simulations, we show for optic vesicles experiencing matrix-constrained growth that elastic instabilities govern the optic cup morphogenesis. By capturing the stress amplification owing to mass increase during growth, we show that the morphogenesis is driven by two elastic instabilities analogous to the snap-through in spherical shells, where the second instability is sensitive to the optic cup geometry. In particular, if the optic vesicle is too slender, it will buckle and break axisymmetry, thus preventing normal development. Our results shed light on the morphogenetic mechanisms governing the formation of a functional biological system, and the role of elastic instabilities in the shape selection of soft biological structures.

Eye development is a complex, multi-scale morphogenetic process that couples cell growth and division, and biological signaling at cellular scales, with large deformation and shape changes. The eye organogenesis begins with formation of the optic vesicles (OV), nearly spherical shells that undergo invagination – a process that locally reverses the curvature of tissues from convex to concave [1], to form the optic cup (OC), a cavity that eventually houses the eye. It is well-established that many congenital eye disorders arise from disruptions in embryonic eye development, including anophthalmia or microphthalmia [2], aniridia [3], coloboma [4], retinal dysplasia [5], and retinal detachment [6].

In the embryonic stage of eye development, the OV bilaterally protrudes from the forebrain and contacts the surface ectoderm (SE). The OV and the SE epithelium are attached to each other through the stiff extracellular matrix (ECM) secreted by both SE and OV, which thickens to form the lens placode and retinal placode. These placodes invaginate, such that curvature of the inner portion of the OV (iOV) changes sign compared to its outer portion (oOV) as shown in Fig. 1a, to form the lens vesicle and OC, respectively [7, 8]. Despite recent efforts [9, 10], important questions remain open as to what mechanisms govern OC morphogenesis during and after invagination [5, 11–17] and how growth of the iOV and oOV, and evolution of their mechanical properties impact the morphogenetic processes.

In this Letter, we advance two novel points that contribute to the physics of OC morphogenesis. First, the morphogenetic process is driven by two elastic instabilities that are analogous to snap-through instabilities in spherical shells. These occur at different times during OC development, corresponding to invagination and rapid deepening observed in biological experiments [13, 18]. Second, we demonstrate that the second morphogenetic instability is sensitive to OC geometry. Specifically, for certain geometries the OC buckles rather than snaps during the second instability, which breaks axisymme-

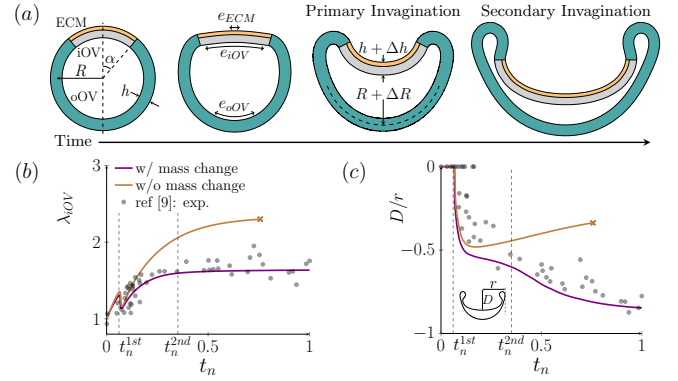


FIG. 1. (a) Simplified schematic of the OC morphogenesis. (b) thickness change ratio of iOV center wall  $\lambda_{iOV}$  as function of the normalized time  $t_n$ . (c) invagination depth  $D$  normalized by OC horizontal radius  $r$  as function of  $t_n$ . (b) and (c) show comparisons of our model with existing experimental data [9], using  $R/h = 5$  and  $\alpha = 40^\circ$  with primary and secondary invagination at  $t_n^{1st}$  and  $t_n^{2nd}$ .

try, and prevents normal OC morphogenesis. This result suggests that some congenital eye disorders, such as glaucoma in newborn infants [19], may be due to OC geometry during morphogenesis.

The OV geometry motivates a simplification of their initial shape to a spherical shell. The ECM and iOV form a bi-layer cap that subtends an *opening angle*  $\alpha$ , while the oOV is a mono-layer covering the rest of the sphere (Fig. 1a). We modeled the mechanical response of the OC as a multi-layer Kirchhoff–Love (KL) shell [20], which assumes the 3D shell may be represented by its 2D mid-surface. Each layer of the KL shell (ECM, iOV, and oOV) is, in contrast to recent works using shells to study biological morphogenesis [21–23], allowed to undergo large strains and rotations and change thickness, via the plane-stress condition, during deformation while being modeled by a compressible neo-Hookean material model [24, 25], which takes the energy density form  $\Psi_0 = \frac{\lambda}{4}(J_m^2 - 1 - 2 \log J_m) + \frac{\mu}{2}(I_{m1} - 3 - 2 \log J_m)$  with Lamé constants  $\lambda$  and  $\mu$ , and invariants  $I_{m1}$  and  $J_m$

of the elastic right Cauchy-Green tensor. To account for large strains and rotations during growth, we utilize the well-established multiplicative decomposition of deformation gradient  $\mathbf{F}$  into growth  $\mathbf{F}_g$  and elastic deformation  $\mathbf{F}_m$  parts [26–29]. Each layer of the OC is subject to isotropic area growth via  $F_g = (e, e, 1)$  where  $e$  is the in-plane expansion factor due to growth [20]. We simulate OC formation process by solving two coupled balance equations: linear momentum balance to determine elastic deformation via  $\mathbf{F}_m$ , and mass balance to account for growth via  $\mathbf{F}_g$ . These equations are solved numerically using the isogeometric analysis (IGA) method, a modern finite element (FE)-like method that is well-suited for shell problems due to its ability to provide an accurate shell mid-surface description [30].

We model the differential growth during OC formation by imposing different mass sources on the ECM, iOV, and oOV in the manner of density-preserving growth [9], such that the three regions have different (experimentally-measured) growth rates [9], i.e.  $e_{ECM}(t_n) = 1$ ,  $e_{iOV}(t_n) = 1 + 5t_n$ , and  $e_{oOV}(t_n) = 1 + 1.5t_n$  as a function of the normalized time  $t_n = t/\tau$ , where  $\tau = 20$  hours is the experimentally measured timescale for OC morphogenesis. The fluid-like components surrounding the OV are neglected [31–33], based on previous studies showing that instabilities of spherical shells are not suppressed by the surrounding fluid environment [34].

A critical, but often neglected, feature in morphogenetic modeling is the effect that mass addition during growth has on the state of stress of the growing body. We find that (see SI for detailed derivation [20]) if the added material during density-preserving growth is the same as the existing material in the body, the stress  $\Sigma^{ij}$  generated in the growing body is amplified as:

$$\Sigma^{ij} = e^2 \frac{\partial \Psi_0}{\partial \epsilon_{ij}} \quad (1)$$

where  $\Psi_0$  is the neo-Hookean strain energy density, and  $\epsilon_{ij}$  is the strain tensor. Thus,  $e^2$  acts as *stress amplification factor* on the internal stress due to mass change from growth, in which  $\partial \Psi_0 / \partial \epsilon_{ij}$  is the standard representation for the internal stress [35]. This stress amplification factor  $e^2$  generalizes previous works [36], as shown in the SI.

We first show that our computational model can capture existing experimental data for OC morphogenesis in a chick embryo [9, 10], as shown in Figs. 1b,c. The geometric and material parameters for the chick OV followed previous experiments [9, 10, 37], i.e. opening angle  $\alpha = 40^\circ$ , initial radius ( $R$ ) of  $50 \mu\text{m}$ , and radius to total thickness ratio ( $R/h$ ) of 5. The bi-layer cap has ECM thickness ( $h^{ECM}$ ) of  $h/10$  and iOV thickness ( $h^{iOV}$ ) of  $9h/10$  whose ratio is  $m = h^{ECM}/h^{iOV} = 1/9$ , and the mono-layer oOV has thickness ( $h^{oOV}$ ) of  $h$ . The shear moduli for the ECM and the iOV and oOV are 11 kPa ( $\mu^{ECM}$ ) and 220 Pa ( $\mu^{iOV}$  and  $\mu^{oOV}$ ), respectively,

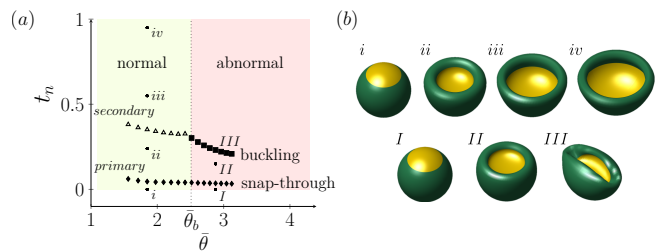


FIG. 2. (a) Simulation results varying  $R/h$  at  $\alpha = 40^\circ$ , considering mass changes. Diamond means the first instability point while triangle and square are the second instability. At  $\bar{\theta} = 2.51$  ( $\bar{\theta}_b$ ), the shape-morphing mechanism changes from secondary invagination (triangle) to buckling (square). (b) Representative OC formation process: normal OC (top row) and abnormal OC shape due to buckling (bottom row).

whose ratio is  $n = \mu^{ECM}/\mu^{iOV} = 50$  on the bi-layer cap. Poisson’s ratio for all regions was set to  $\nu = 0.45$  based on biologically observed data showing that eye tissue is not incompressible [38, 39].

Figs. 1b,c show the simulation results of OC formation with and without accounting for the effect of mass change during growth on the stress, where neglecting the mass change corresponds to taking  $e^2 \rightarrow 1$  in (1). By comparing to the experimental results [9], it is clear that our model accurately captures the evolution of thickness change ratio of iOV center wall ( $\lambda_{iOV}$ ) as well as invagination depth ( $D$ ) normalized by OC horizontal radius ( $r$ ), which are geometric parameters that characterize the OC size and shape. Therefore, the stress amplification from mass addition significantly impacts the local and inhomogeneous growth and enables the accurate simulation of experimentally-observed OC growth. This also demonstrates that there is no need to prescribe hypothetical stiffness or growth property gradients as in previous OC growth modeling [9, 10].

The OV thickness is known to vary with diverse biological cues, such as protein-2 alpha [40–42], which implies that the radius-thickness ratio  $R/h$  of initial OC shape also varies with different biological situations. To account for these unknown thickness variations, we performed numerical simulations at  $\alpha = 40^\circ$  with different  $R/h$  within the biologically relevant range (5 to 20) [43–45]. This initial geometry is characterized using a single, dimensionless parameter  $\bar{\theta} = \alpha\sqrt{R/h}$ , which describes the depth and slenderness of the bi-layer cap region relative to the angular width of boundary layer [46].

For all values of  $\bar{\theta}$  examined, the shells exhibit two distinct shape-shifting events (Fig. 2). At early times, the apex of the OC inverts, resulting in formation of a cup-like shape, which we refer to as *primary invagination* (Fig. 2,  $i \rightarrow ii$ ,  $I \rightarrow II$ ). As  $t_n$  increases, we observe a second shape-shifting event that is sensitive to the initial geometry. For lower  $\bar{\theta}$ , i.e. thicker shells, we observe a rapid deepening of the OC which preserves axisymmetry – we refer to this as *secondary invagination* (Fig. 2,  $ii \rightarrow iii$ ). For higher  $\bar{\theta}$ , i.e. thinner shells, we observe

that the second shape-shifting event consists of a loss of axisymmetry (Fig. 2, *II*  $\rightarrow$  *III*). We note that for simulations that neglect mass changes, the symmetry-breaking event (*II*  $\rightarrow$  *III*) occurred for all  $\bar{\theta}$ , which means the normal morphogenesis process resulting in an axisymmetric OC cannot be modeled without mass addition. See SI for OC formation movies.

To analyze, rationalize, and predict the qualitative features underlying the different shape-morphing pathways of OC morphogenesis, we used a shell model which accounts for growth as a stimulus that changes the rest length, i.e. *natural stretch*, and curvature, i.e. *natural curvature* of the shell's mid-surface. The strain energy stored in the shell during growth is estimated based on *updated rest mid-surfaces*. As a result, the natural curvature in the cap acts like a torque along the intersection between the cap and oOV to deform the OC [20]. When these natural quantities are homogeneous over some segment of shells, they can be represented by scalar values of  $\Lambda$  (stretch) and  $\kappa$  (curvature) whose specific values are calculated for each segment of the OC based on the experimentally-measured growth characteristics (see SI for detailed derivation [20]), i.e.  $e_{ECM}$  and  $e_{iOV}$  for the bi-layer cap, and  $e_{oOV}$  for the oOV. As a result, the cap and oOV have their own scalar values of natural stretch and curvature. The presence of  $\Lambda$  and  $\kappa$  imparts residual stresses in the growing OC, and these quantities play a similar role as external loads and torques do in classical mechanics, which can destabilize shells [47, 48]. This suggests that OC morphogenesis may be governed by instabilities which result from residual stress that builds up during growth.

In the cap region, experimental observations note that the ECM and iOV grow at different rates. This through-thickness differential growth induces a natural curvature that changes the apex of the OC from convex to concave. However, the inversion of this cap is resisted by the oOV which is a mono-layer growing homogeneously and has to bend to accommodate the deforming cap. Open spherical shells experiencing an evolving natural curvature may exhibit a snap-through instability that everts the shell at a critical curvature [47]. Here, the OC is not an open shell, as the deformation of the cap will be resisted by the oOV. However, since the oOV is resisting bending, and therefore resisting rotations imparted by the growth-induced torque along the intersection, we treated the oOV as an *effective* rotational spring (Fig. 3a). Therefore, by way of a simple mechanical analogy, we model the full OC as an open spherical shallow shell, whose geometry is the same as the bi-layer cap, experiencing an equivalent edge torque as shown in Fig. 3a. The natural curvature in the cap due to differential growth,  $\kappa^{cap}$ , has to overcome the bending rigidity of the effective rotational spring [20],

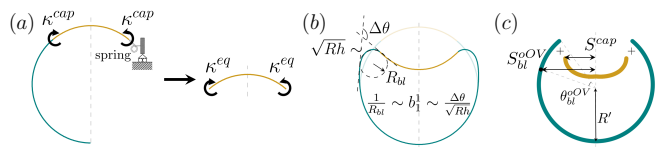


FIG. 3. (a) Equivalent natural curvature. (b) Geometrical characteristics on the oOV bending-dominated boundary layer. (c) Characteristic span of each separated cap and oOV.

resulting in an *equivalent* natural curvature given by

$$\kappa^{eq} \sim \kappa^{cap} - \Gamma \frac{\Delta\theta}{\sqrt{Rh}} \quad (2)$$

where  $\Gamma$  is a dimensionless ratio of bending rigidities, i.e.  $\Gamma = \frac{B^{oOV}}{2B^{cap}(1+\nu)}$  ( $\Gamma = 0.06$  for the OC) with bending rigidities  $B^{cap}$  and  $B^{oOV}$  of the cap and oOV, respectively, and  $\Delta\theta$  is angle change along the oOV boundary layer as shown in Fig. 3b. Here, we assumed most of the oOV deformation occurs within its boundary layer as bending [49], and the second term on RHS of (2) describes the amount that acts to bend the oOV boundary layer.

Open spherical shallow shells undergo snapping under homogeneous positive natural curvature when the boundary tangent vector in the colatitude direction becomes approximately horizontal, which results in  $\kappa^{eq}R \sim \bar{\theta}$  at the snapping [47]. Our numerical experiments here on closed spherical shells exhibit qualitatively similar behavior when the primary invagination occurs via snapping. That is, the primary invagination occurs when the colatitude-direction tangent vector at the intersection between the cap and oOV becomes approximately horizontal, which leads to  $\Delta\theta \sim \alpha$  in (2) at the primary invagination. This results in a scaling law of the critical natural curvature in the cap at the primary invagination as

$$\kappa_1^{cap}R = a_1(1 + \Gamma)\bar{\theta} + b_1 \quad (3)$$

where  $a_1$  and  $b_1$  are scaling coefficients determined by our numerical simulations, which confirms the linear scaling with  $\bar{\theta}$ , and identifies the scaling coefficients as  $a_1 = 1.55$  and  $b_1 = -0.95$  (black solid line in Fig. 4a). As with open shells, the primary invagination via snapping will only occur if  $\bar{\theta} > \bar{\theta}_s (= [10/(1 - \nu^2)]^{1/4})$  where  $\bar{\theta}_s = 1.88$  for the OC [20], in good agreement with prior work [47] as the bending-dominated boundary layer covers the entire shell for  $\bar{\theta} < \bar{\theta}_s$ .

Following this primary invagination, growth and development of the OC continue until a second shape-shifting event occurs, which appears to be strongly correlated to the OC geometry. Thicker shells undergo a secondary invagination, forming a deep cup that facilitates normal eye development, while slender shells lose axisymmetry, forming a shape that may hinder normal OC morphogenesis. First, we consider the onset of secondary invagination. The magnitude of the torque at the intersection

between the cap and oOV continues to increase due to the continued differential growth of the ECM and iOV. The oOV is not rigid, and therefore the torque can either bend the oOV or further bend the cap. Building on the concept of a geometric composite [50], we can consider the growing cap and oOV as separate structures, and then determine how they will deform when combined together. The cap, when removed from the OC, would form a shallow shell that spans a characteristic distance  $S^{cap}$  (Fig. 3c – yellow). The oOV, when removed from the OC, would form a deep spherical shell of radius  $R' = e_{oOV}R$ , which is current radius as a result of growth. From our numerical simulations, we note that the extent of the oOV boundary layer, where bending deformations are concentrated, is constant until the secondary invagination occurs. We can estimate the characteristic span  $S_{bl}^{oOV}$  of the oOV from the extent of its boundary layer (Fig. 3c – blue), and observe that during secondary invagination the oOV boundary layer increases in length and curvature. Therefore, we posit that when the span of the cap exceeds the span of the oOV boundary layer, the OC will undergo secondary invagination to account for this excess length.

The characteristic span of this oOV segment scales as  $S_{bl}^{oOV} \sim R' \sin(\alpha + \theta_{bl}^{oOV})$  where  $\theta_{bl}^{oOV}$  is angle subtended by the oOV boundary layer, which scales as  $\theta_{bl}^{oOV} \sim \sqrt{h/R}$  for spherical shells [46]. The span of the cap scales as  $S^{cap} \sim R\alpha(1 + \chi(1 + \nu)h\kappa^{cap})$ , where  $\chi = (1 + m(3n - 2))/(6mn)$  [20]. If we suppose that the critical point occurs when the spans are equivalent, *i.e.*  $S_{bl}^{oOV} = S^{cap}$ , we obtain that the critical natural curvature is proportional to the shell geometry as  $\kappa^{cap}R \propto R/h$  from which the critical natural curvature in the cap at secondary invagination can be estimated as

$$\kappa_2^{cap}R \propto \frac{R}{h} = a_2 \frac{\bar{\theta}^2}{\alpha^2} + b_2, \quad (4)$$

where  $a_2$  and  $b_2$  are obtained from simulations to be  $a_2 = 0.86$  and  $b_2 = 0.22$ . These parameters capture well the secondary invagination via the dashed color line in Fig. 4a. Notably, unlike the primary invagination given by (3), the secondary invagination depends on opening angle  $\alpha$ .

While our model predicts the morphogenetic process of OC formation via the experimentally-observed [9, 10] two-step (primary and secondary) invagination, it also indicates that very slender initial OC geometries will undergo an elastic instability that breaks axisymmetry, leading to abnormal OC development. This loss of the OC axisymmetry has been observed for glaucoma in newborn infants [19]. Secondary invagination occurs when the oOV boundary layer is flexible enough to bend to accommodate the excess length of the growing cap. If the oOV is too stiff, the cap must bend instead. If we presume that the loss of axisymmetry for slender optic cups is due to a buckling instability, then the critical nat-

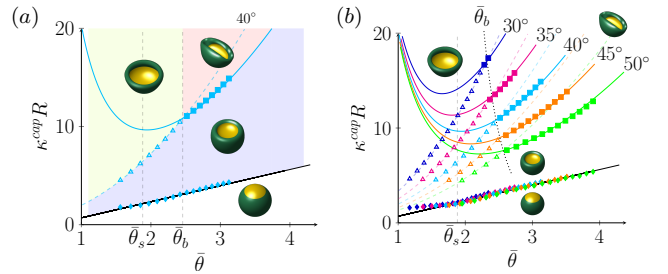


FIG. 4. (a) Phase diagram of instabilities during OC formation for varying  $R/h$  at  $\alpha = 40^\circ$ . The blue region denotes the invaginated cup shape, and the lime and red regions are the normal (secondary invagination) and abnormal (buckling) OC, respectively. (b) Phase diagram for varying  $R/h$  and  $\alpha$ . For (a) and (b), the symbols refer to simulation results, with diamonds symbolizing primary invagination, triangles for secondary invagination, and squares for buckling. The lines represent the scaling law of (3), (4) and (5). The black dotted line in (b) shows the buckling transition point  $\bar{\theta}_b$  of (6).

ural curvature can be analytically calculated via a linear stability analysis, which for a circular plate with natural curvature  $\kappa^p$  and radius  $R^p$  gives  $\kappa^p h = \pm a_b (h/R^p)^2$  with  $a_b = \chi(5 + 3\nu)/(1 - \nu^2)$  at the buckling instability ( $a_b = 4.17$  for the OC) [20]. To connect this critical natural curvature to open spherical shallow shells, we substitute  $R^p \rightarrow R\alpha$ . This gives us  $\kappa^{eq}R \sim a_b/\bar{\theta}^2 + 1$ , which is similar to [47]. Furthermore, the spherical shell's geometry under a torque induced by natural curvature leads to  $\Delta\theta \sim \sqrt{R/h}$  in (2) at the buckling instability [20]. Then, the critical natural curvature in the cap at the buckling instability is given by

$$\kappa_b^{cap}R = b_b \left( \frac{a_b}{\bar{\theta}^2} + 1 + \Gamma\alpha_2 \frac{\bar{\theta}^2}{\alpha^2} \right) + c_b \quad (5)$$

where  $\alpha_2 (= \pi - \alpha)$  is a prefactor to treat the deep oOV shell, and  $b_b$  and  $c_b$  are scaling coefficients which provide the best fit with our simulations through  $b_b = 4.72$  and  $c_b = -5.50$  via the solid color line in Fig. 4a.

As our numerical experiments indicate that both secondary invagination and symmetry-breaking buckling cannot occur for the same initial geometry, the intersection between (4) and (5) gives us the transition point from secondary invagination to buckling as

$$\bar{\theta}_b = \sqrt{\frac{\sqrt{4\alpha^2 b_b a_b (a_2 - \alpha_2 b_b \Gamma) + \alpha^4 (c_b - b_2 + b_b)^2} + \alpha^2 (c_b - b_2 + b_b)}{2(a_2 - \alpha_2 b_b \Gamma)}} \quad (6)$$

where  $\bar{\theta}_b = 2.46$  is calculated at  $\alpha = 40^\circ$ , in agreement with the numerical results ( $\bar{\theta}_b = 2.51$ ).

Similar to the various  $R/h$  in biological situations, it is natural to think that the opening angle will also vary with diverse biological cues. The simulation results with various opening angles for a wide range from  $30^\circ$  to  $50^\circ$  are plotted on a phase diagram in Fig. 4b which fully characterizes the instability-induced shape-morphing of the OC during its morphogenesis for a variety of initial

geometries, showing that the proposed scaling laws work well for all  $\alpha$ . Above the value of  $\bar{\theta}_b$ , denoted as the dashed black line via (6), the final OC shape is abnormal for each  $\alpha$ .

In summary, we revealed the significant role that elastic instabilities play during OC morphogenesis. Because our model is predictive based on the initial geometry, we hope that our study will motivate experimental efforts to measure radius  $R$ , thickness  $h$ , and opening angle  $\alpha$  of the initial OV to investigate their effects on OC morphogenesis and to verify the accuracy of our model predictions.

JHL, HSP, and DPH gratefully acknowledge the financial support from the National Science Foundation through CMMI-1824882.

---

\* parkhs@bu.edu

† dpholmes@bu.edu

- [1] E. J. Pearl, J. Li, and J. B. Green, Cellular systems for epithelial invagination, *Philosophical Transactions of the Royal Society B: Biological Sciences* **372**, 20150526 (2017).
- [2] S. E. Skalicky, A. J. White, J. R. Grigg, F. Martin, J. Smith, M. Jones, C. Donaldson, J. E. Smith, M. Flaherty, and R. V. Jamieson, Microphthalmia, anophthalmia, and coloboma and associated ocular and systemic features: understanding the spectrum, *JAMA ophthalmology* **131**, 1517 (2013).
- [3] H. Lee, R. Khan, and M. OKeefe, Aniridia: current pathology and management, *Acta ophthalmologica* **86**, 708 (2008).
- [4] C.-J. Zhou, A. Molotkov, L. Song, Y. Li, D. E. Pleasure, S. J. Pleasure, and Y.-Z. Wang, Ocular coloboma and dorsoventral neuroretinal patterning defects in *lrp6* mutant eyes, *Developmental dynamics: an official publication of the American Association of Anatomists* **237**, 3681 (2008).
- [5] S. Fuhrmann, Eye morphogenesis and patterning of the optic vesicle, in *Current topics in developmental biology*, Vol. 93 (Elsevier, 2010) pp. 61–84.
- [6] D. Rosen and N. Mahabadi, Embryology, optic cup, in *StatPearls [Internet]* (StatPearls Publishing, 2019).
- [7] R. Hendrix and J. Zwaan, Changes in the glycoprotein concentration of the extracellular matrix between lens and optic vesicle associated with early lens differentiation, *Differentiation* **2**, 357 (1974).
- [8] C. D. Bryan, M. A. Casey, R. L. Pfeiffer, B. W. Jones, and K. M. Kwan, Optic cup morphogenesis requires neural crest-mediated basement membrane assembly, *Development* **147** (2020).
- [9] A. Oltean, J. Huang, D. C. Beebe, and L. A. Taber, Tissue growth constrained by extracellular matrix drives invagination during optic cup morphogenesis, *Biomechanics and modeling in mechanobiology* **15**, 1405 (2016).
- [10] H. S. Hosseini and L. A. Taber, How mechanical forces shape the developing eye, *Progress in biophysics and molecular biology* **137**, 25 (2018).
- [11] R. Adler and M. V. Canto-Soler, Molecular mechanisms of optic vesicle development: complexities, ambiguities and controversies, *Development Biology* **305**, 1 (2007).
- [12] J. Hyer, J. Kuhlman, E. Afif, and T. Mikawa, Optic cup morphogenesis requires pre-lens ectoderm but not lens differentiation, *Developmental biology* **259**, 351 (2003).
- [13] M. Eiraku, N. Takata, H. Ishibashi, M. Kawada, E. Sakakura, S. Okuda, K. Sekiguchi, T. Adachi, and Y. Sasai, Self-organizing optic-cup morphogenesis in three-dimensional culture, *Nature* **472**, 51 (2011).
- [14] T. Nakano, S. Ando, N. Takata, M. Kawada, K. Mugeruma, K. Sekiguchi, K. Saito, S. Yonemura, M. Eiraku, and Y. Sasai, Self-formation of optic cups and storable stratified neural retina from human *escs*, *Cell stem cell* **10**, 771 (2012).
- [15] K. M. Kwan, H. Otsuna, H. Kidokoro, K. R. Carney, Y. Saijoh, and C.-B. Chien, A complex choreography of cell movements shapes the vertebrate eye, *Development* **139**, 359 (2012).
- [16] W. A. Harris and V. Hartenstein, Neuronal determination without cell division in *xenopus* embryos, *Neuron* **6**, 499 (1991).
- [17] J. R. Martinez-Morales and J. Wittbrodt, Shaping the vertebrate eye, *Current opinion in genetics & development* **19**, 511 (2009).
- [18] S. Okuda, N. Takata, Y. Hasegawa, M. Kawada, Y. Inoue, T. Adachi, Y. Sasai, and M. Eiraku, Strain-triggered mechanical feedback in self-organizing optic-cup morphogenesis, *Science advances* **4**, eaau1354 (2018).
- [19] K. T. Richardson, Optic cup symmetry in normal newborn infants, *Investigative Ophthalmology & Visual Science* **7**, 137 (1968).
- [20] See Supplemental Material at [URL will be inserted by publisher] for a detailed derivation, which includes Refs. [51–58].
- [21] S. Höhn, A. R. Honerkamp-Smith, P. A. Haas, P. K. Trong, and R. E. Goldstein, Dynamics of a *volvax* embryo turning itself inside out, *Physical review letters* **114**, 178101 (2015).
- [22] P. A. Haas, S. M. H. Hohn, A. R. Honerkamp-Smith, J. B. Kirkegaard, and R. E. Goldstein, The noisy basis of morphogenesis: mechanisms and mechanics of cell sheet folding inferred from development variability, *PLOS Biology* **16**, e2005536 (2018).
- [23] P. A. Haas and R. E. Goldstein, Morphoelasticity of large bending deformations of cell sheets during development, *Physical Review E* **103**, 022411 (2021).
- [24] G. Chagnon, M. Rebouah, and D. Favier, Hyperelastic energy densities for soft biological tissues: a review, *Journal of Elasticity* **120**, 129 (2015).
- [25] S. Budday, G. Sommer, C. Birkel, C. Langkammer, J. Haybaeck, J. Kohnert, M. Bauer, F. Paulsen, P. Steinmann, E. Kuhl, *et al.*, Mechanical characterization of human brain tissue, *Acta biomaterialia* **48**, 319 (2017).
- [26] E. K. Rodriguez, A. Hoger, and A. D. McCulloch, Stress-dependent finite growth in soft elastic tissues, *Journal of biomechanics* **27**, 455 (1994).
- [27] A. Goriely, *The mathematics and mechanics of biological growth*, Vol. 45 (Springer, 2017).
- [28] E. Kuhl, *Growing matter: a review of growth in living systems* (2014).
- [29] V. A. Lubarda and A. Hoger, On the mechanics of solids with a growing mass, *International journal of solids and structures* **39**, 4627 (2002).

- [30] T. X. Duong, F. Roohbakhshan, and R. A. Sauer, A new rotation-free isogeometric thin shell formulation and a corresponding continuity constraint for patch boundaries, *Computer Methods in applied Mechanics and engineering* **316**, 43 (2017).
- [31] A. V. De Reuck and J. Knight, *Colour vision: Physiology and experimental psychology*, Vol. 965 (John Wiley & Sons, 2009).
- [32] S. R. Hilfer, R. C. Brady, and J.-J. W. Yang, Intracellular and extracellular changes during early ocular development in the chick embryo, in *Ocular Size and Shape Regulation During Development* (Springer, 1981) pp. 47–78.
- [33] H. S. Hosseini, D. C. Beebe, and L. A. Taber, Mechanical effects of the surface ectoderm on optic vesicle morphogenesis in the chick embryo, *Journal of biomechanics* **47**, 3837 (2014).
- [34] A. Djellouli, P. Marmottant, H. Djeridi, C. Quilliet, and G. Couplier, Buckling instability causes inertial thrust for spherical swimmers at all scales, *Physical review letters* **119**, 224501 (2017).
- [35] A. G. Holzapfel, *Nonlinear solid mechanics ii*, (2000).
- [36] M. Ben Amar and A. Goriely, Growth and instability in elastic tissues, *Journal of the Mechanics and Physics of Solids* **53**, 2284 (2005).
- [37] G. Xu, P. S. Kemp, J. A. Hwu, A. M. Beagley, P. V. Bayly, and L. A. Taber, Opening angles and material properties of the early embryonic chick brain, *Journal of biomechanical engineering* **132** (2010).
- [38] E. Uchio, S. Ohno, J. Kudoh, K. Aoki, and L. T. Kisielewicz, Simulation model of an eyeball based on finite element analysis on a supercomputer, *British Journal of Ophthalmology* **83**, 1106 (1999).
- [39] I. A. Sigal, J. G. Flanagan, and C. R. Ethier, Factors influencing optic nerve head biomechanics, *Investigative ophthalmology & visual science* **46**, 4189 (2005).
- [40] E. A. Bassett, T. Williams, A. L. Zacharias, P. J. Gage, S. Fuhrmann, and J. A. West-Mays, *Ap-2 $\alpha$*  knockout mice exhibit optic cup patterning defects and failure of optic stalk morphogenesis, *Human molecular genetics* **19**, 1791 (2010).
- [41] L.-Y. Wu, M. Li, D. R. Hinton, L. Guo, S. Jiang, J. T. Wang, A. Zeng, J. B. Xie, M. Snead, C. Shuler, *et al.*, Microphthalmia resulting from *msx2*-induced apoptosis in the optic vesicle, *Investigative ophthalmology & visual science* **44**, 2404 (2003).
- [42] Y. Ishii, K. Weinberg, I. Oda-Ishii, L. Coughlin, and T. Mikawa, Morphogenesis and cytodifferentiation of the avian retinal pigmented epithelium require downregulation of group b1 sox genes, *Development* **136**, 2579 (2009).
- [43] F. Müller, H. Rohrer, and A. Vogel-Höpker, Bone morphogenetic proteins specify the retinal pigment epithelium in the chick embryo, *Development* **134**, 3483 (2007).
- [44] T. Pandit, V. K. Jidigam, C. Patthey, and L. Gunhaga, Neural retina identity is specified by lens-derived bmp signals, *Development* **142**, 1850 (2015).
- [45] Y. Hasegawa, N. Takata, S. Okuda, M. Kawada, M. Eiraku, and Y. Sasai, Emergence of dorsal-ventral polarity in *esc*-derived retinal tissue, *Development* **143**, 3895 (2016).
- [46] F. I. Niordson, *Shell theory* (Elsevier, 2012).
- [47] M. Pezzulla, N. Stoop, M. P. Steranka, A. J. Bade, and D. P. Holmes, Curvature-induced instabilities of shells, *Physical review letters* **120**, 048002 (2018).
- [48] D. P. Holmes, J.-H. Lee, H. S. Park, and M. Pezzulla, Nonlinear buckling behavior of a complete spherical shell under uniform external pressure and homogenous natural curvature, *Physical Review E* **102**, 023003 (2020).
- [49] E. Efrati, E. Sharon, and R. Kupferman, Buckling transition and boundary layer in non-euclidean plates, *Physical Review E* **80**, 016602 (2009).
- [50] M. Pezzulla, S. A. Shillig, P. Nardinocchi, and D. P. Holmes, Morphing of geometric composites via residual swelling, *Soft Matter* **11**, 5812 (2015).
- [51] R. A. Sauer and T. X. Duong, On the theoretical foundations of thin solid and liquid shells, *Mathematics and mechanics of solids* **22**, 343 (2017).
- [52] F. Roohbakhshan and R. A. Sauer, Efficient isogeometric thin shell formulations for soft biological materials, *Biomechanics and modeling in mechanobiology* **16**, 1569 (2017).
- [53] E. Efrati, E. Sharon, and R. Kupferman, Elastic theory of unconstrained non-euclidean plates, *Journal of the Mechanics and Physics of Solids* **57**, 762 (2009).
- [54] W. T. Koiter and J. G. Simmonds, Foundations of shell theory, in *Theoretical and applied mechanics* (Springer, 1973) pp. 150–176.
- [55] M. Pezzulla, N. Stoop, X. Jiang, and D. P. Holmes, Curvature-driven morphing of non-euclidean shells, *Proceedings of the Royal Society A: Mathematical, Physical and Engineering Sciences* **473**, 20170087 (2017).
- [56] A. Lucantonio, P. Nardinocchi, and M. Pezzulla, Swelling-induced and controlled curving in layered gel beams, *Proceedings of the Royal Society A: Mathematical, Physical and Engineering Sciences* **470**, 20140467 (2014).
- [57] M. Pezzulla, G. P. Smith, P. Nardinocchi, and D. P. Holmes, Geometry and mechanics of thin growing bilayers, *Soft Matter* **12**, 4435 (2016).
- [58] W. T. Koiter and A. Van Der Heijden, *WT Koiter's elastic stability of solids and structures* (Cambridge University Press Cambridge, UK; New York, NY, USA, 2009).